G. PRABU[1], MUTHUKANNAN DURAISELVAM[1*]

TRIBOLOGICAL STUDIES ON ALCRFECUCONI HIGH ENTROPY ALLOY SURFACE COATED ON TI-6AL-4V USING PLASMA TRANSFERRED ARC TECHNIQUE

AlCrFeCuCoNi high entropy particles were alloyed on Ti-6Al-4V surface using Plasma transferred arc (PTA) process. PTA alloyed surfaces were investigated for their phase formation, microhardness improvement and wear behaviour. The various wear mechanism and their corresponding surface roughness were studied. The results revealed that the dual phase of BCC and FCC microstructure along with some intermetallic compounds were grown in the alloyed region through the PTA technique and good metallurgical bonding of the alloyed region with the base material were achieved. The PTA alloyed region exhibited a hardness of 718 $HV_{0.2}$ which is 2.2 times higher than the hardness of base material. The PTA alloyed samples showed higher wear resistance due to the solid solution strengthening as the HEA has high entropy of mixing that leads to the reduction of free energy of the alloyed region. It exhibited better interconnection of the coated material and superior metallurgical bonding to the base material. Frictional heat produced during the wear test has promoted the formation of FeO, Cr_2O_3, CuO, NiO and Al_2O_3 oxide film on the PTA alloyed sample. These oxide films act as a barrier between two mating surfaces and improve the tribo performance of the PTA alloyed sample.

Keywords: Titanium alloy; High entropy alloy; Plasma transferred arc (PTA); Alloying; Wear mechanism

1. Introduction

Titanium based alloys are commonly used in automobile, marine, aerospace, power generation, biomedical and chemical industries due to their excellent properties such as high specific strength, low weight, good biocompatibility, excellent corrosion and oxidation resistance [1]. However, the usage of titanium alloys was limited due to poor wear resistance [2]. The increase in material loss due to higher frictional force and greater impact on the sliding surfaces is basically a surface-related phenomenon. The material removal is mainly depending on the elemental composition and material structure of the top surface. Therefore, a suitable surface modification needs to be implemented to protect from undesired material loss. In recent years, many surface modification techniques were attempted to improve the surface properties of titanium alloys such as chemical vapour deposition, physical vapour deposition, micro-arc oxidation, electroplating, laser modification and plasma transferred arc (PTA) process [3-9]. Among these techniques, PTA based surface modification was attracted much attention due to high efficiency, good metallurgical bond, low cost and easy operation.

Youlu Yuan and Zhuguo Li [10] studied the wear behavior of WC/Fe coating on mild steel using PTA technique. Results indicated that WC content directly increases the anti-wear property with improved hardness. Garcia et al. [11] investigated the micro-abrasion and corrosion behavior of NiCr coating using the PTA process. The outcome showed that the wear coefficients which were measured under micro-abrasion and corrosion condition were improved. Baiamonte et al. [12] examined the tribological and mechanical properties of stellite coated steel using the PTA method. Results indicated that the hardness and wear resistance of the deposition was improved. Cao et al. [13] studied the wear behavior of high vanadium steel coating on an iron surface using PTA alloying. Results showed that the microhardness and wear resistance of the alloyed sample was improved due to the rapid solidification of the PTA process.

High entropy alloy (HEA) is a new form of material composition to meet the functional properties such as hardness, corrosion and wear resistance over conventional alloys [14]. HEA can be prepared by mixing more than or equal to five elements at an equal or non-equal molar ratio. The stability of solution phases is increased due to high mixing entropy, cocktail effect,

[1] NATIONAL INSTITUTE OF TECHNOLOGY, DEPARTMENT OF PRODUCTION ENGINEERING, TIRUCHIRAPPALLI, INDIA

* Corresponding author: durai@nitt.edu

lattice distortion and sluggish diffusion of HEAs which leads to a decrease in Gibbs free energy. Dechao Zhao et al. [15] recently synthesized $Al_{0.8}FeCrCoNi$ HEA coating on magnesium alloy using resistance seam welding (RESW) heat source. The wear properties were studied in three different environments and concluded that the surface-modified magnesium alloy showed superior wear resistance. Hao Liua et al. [16] prepared AlCoCrFeNiTi$_x$ HEA coating on steel surface through laser cladding and studied the wear properties of the coating. Results showed that the HEA alloy surface exhibited higher wear resistance compared to the base material. Huebner et al. [17] studied the wear behaviour of laser alloyed WC-Co particles on nodular iron and concluded that the hardness and wear properties were improved compared to the base material.

AlCoCrFeNi quinary HEA alloys possess single solid solution whereas AlCoCrCuFeNi six-element HEA alloys possess dual phases of BCC and FCC. This dual-phase has protected the surface from abrasive and adhesive wear by the hard BCC phase and avoid brittle fracture by tough FCC phase. ΔS_{mixing} = R ln (number of elements mixing) = R ln 6 = 1.79R (where, ΔS_{mixing} is change in mixing entropy, R is the gas constant). It shows that the high entropy is formed by mixing of six elements than the mixing of five elements [18]. The mixing entropy is higher than the entropy of the intermetallic compound. It leads to the formation of single or dual phase than the intermetallic phases. Guo et al. [19] studied the wear behavior of FeNiCoAlCu high entropy alloy coating. It was found that oxides such as CuO, Fe_3O_4 were formed on the HEA coated surface which was protected the coated surface from aggressive wear. Cu element in AlCrFeCuCoNi HEA can act as effective lubrication, maintain antifouling properties, reduce embrittlement and improve tribological properties. The plastic deformation and delamination were reduced during the tribological study. Benbin et al. [20] fabricated the composite coating of $Cu/MoO_3/NiCrAlY/Cr_3C_2(NiCr)$ on GH4169 alloy and analyzed the tribological property. The results revealed that CuO and NiO were formed on the coated surface and enhanced the anti-wear property due to its self-lubrication characteristics. Jiasi et al. [21] have added 3 wt.% Cu and found that Cu addition enhanced both corrosion resistant wear resistance property of CoCrW alloys. Based on the above literature, the addition of Cu element to quinary elements such as Al, Cr, Fe, Co and Ni would enhance the tribological property. Hence, in the present study Al, Cr, Fe, Cu, Co and Ni are selected. The difference between the atomic size of the alloying elements are less. These alloying elements have the ability to mutually substitute with one another. As a result, AlCrFeCuCoNi HEA has excellent properties and many potential applications.

There is no literature was found on surface alloying of AlCrFeCuCoNi high entropy particles on Ti-6Al-4V material using plasma transferred arc technique. In the present study, AlCrFeCuCoNi HEA powders were preplaced on the Ti-6Al-4V and surface alloyed through the PTA technique. PTA alloyed surfaces were investigated for their phase formation, improvement in hardness and wear behaviour. The various wear mechanism and their corresponding surface roughness were experimentally studied.

2. Experimental procedure

2.1. Base material and alloy powder

Ti-6Al-4V titanium alloy with the dimension of $50 \times 50 \times 15$ mm was used as a base material and the chemical composition is shown in Table 1. The surface of the base material was sandblasted with a minimum roughness of 7 μm to achieve good adhesiveness of coated particles. The sample surface was cleaned with acetone and the compressed hot air was used to dry the specimen. The high purity powders such as Al, Co, Cr, Cu, Fe and Ni elements were purchased from Well-Being Enterprise Co. Ltd, India. The powders were taken at equal atomic ratio and mixed using ball milling machine (VBCC, High Energy Planetary Ball Mill, India). The system consisted of one cylindrical tank and spherical balls. It was operated at a rotating speed of 220 RPM for a milling period of 16 hours with 5 min break for every 4 h operation time. Stainless steel (SS) balls of 6mm diameter were used in the ball milling process, where the mass ratio of SS-ball to powder was taken as 10:1. Prior to the ball milling process, SS cylindrical tank was evacuated and filled with pure argon gas for providing the controlled atmosphere during the ball milling process. The cylindrical tank and balls were rotated in the opposite direction with each other. The ball was rotating about its own axis as well as rotated inside the cylindrical tank due the rotation of cylindrical tank. During this operation, the centrifugal force was created by the ball which was used to fracture the HEA particle. As a result of the ball milling process, agglomeration of HEA particles were avoided and the powder was mixed uniformly.

TABLE 1

Chemical composition of Ti-6Al-4V

Elements	Ti	Al	V	Fe	O	C	N
Wt (%)	Bal.	5.69	4.02	0.21	0.22	0.07	0.04

2.2. Preplaced coating and PTA alloying

Polyvinyl Alcohol (PVA) was mixed with distilled water in the ratio of 15: 85, and boiled up to 300°C. The milled powder was added with PVA and magnetically stirred for 3 hours to make a thick paste. The thick paste of alloy powders was preplaced on the Ti-6Al-4V surface with a uniform thickness of 500 μm and the coated specimen was kept in a fume cupboard for 35 h to dry the deposited layers. The preplaced specimens were PTA processed with a high energy flame (PTAW-A-001, Power Technologies, India). The Fig. 1 shows the schematic representation of the PTA alloying process. It consisted of tungsten electrode which act as a cathode electrode and is connected to negative terminal. Nozzle of the gun is connected to the positive terminal and act as an anode electrode. The mixture of gas is supplied to the nozzle to produce the strong arc between the electrodes. Electrons from the arc collided with the gas molecules and

resulted in disassociation of molecules into individual atoms. Moreover, these atoms further split into electrons and ions due to high temperature gradient of arc. As a result, electrically charged ions are formed which shows that the gas is converted in to a plasma. During this ionization process, more amount of heat is liberated between nozzle and specimen. These high temperature of plasma (ionized gas) move at high velocity towards the HEA coated surface. Pure argon gas was used during the PTA process to avoid atmospheric contamination. The prepared test specimens were irradiated at various PTA parameters to identify the optimal processing parameter. Table 2 shows the optimal PTA parameters which are used in the present study.
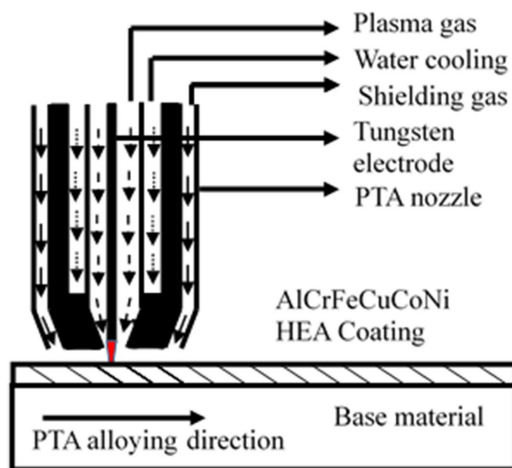

Fig. 1. Schematic representation of PTA alloying setup

TABLE 2

Optimized parameter of PTA process

Parameters	Value
Arc current (A)	115
Arc Voltage (V)	23.9
Nozzle height from sample (mm)	5.5
Scanning speed (mm/s)	1.5
Shroud gas	Argon
Shield gas flow rate (lpm)	12
Centre Gas (lpm)	1.8
Defection Angle (deg)	90°
Overlapping (%)	25

2.3. Wear study and characterizations

The PTA alloyed specimens were cut in cross-section for X-ray diffraction (XRD) analysis, microstructure and hardness investigation. The cross-sectioned specimens were polished using various emery sheet followed by cloth polishing. Aqua regia acid was used as chemical etchant to reveal the structure of the PTA surface which is prepared by mixing HNO and HCl acid in the ratio of 1:3. The phase composition of ball-milled powder and PTA alloyed samples were examined using Cu Kα radiated X-ray diffraction (D/MAX/2200/PC Ultima IV, Regaku, Japan)

with the operating current and voltage of 30 mA and 40 kV, respectively. The microstructure of base material and PTA alloyed cross-section were examined through Optical microscope (OM) (BX41M-LED, Olympus, Japan) and Field emission scanning electron microscopy (Sigma Gemini Column, Carl Zeiss, USA) (FESEM). Microhardness test was performed with 200 g load and 15s dwell time to study the hardness variation on base material and PTA alloyed surface using Vickers microhardness tester (402 MVD, Wolpert Wilson Instruments, USA). Sliding wear tests were conducted using pin-on-disc wear test machine (TR-20LE-PHM 400-CHM 500, Ducom Instruments, India) as per ASTM G99-05 standard [22]. PTA alloyed samples with the dimension of $6 \times 6 \times 15$ mm were used as pin whereas the hardened steel with 8 mm thickness and 100 mm diameter was used as a counterpart. Dry sliding wear test was performed at 35 N and 50 N load and with the sliding velocity of 0.9 m/s and 1.2 m/s with a constant sliding distance of 1000 m and at room temperature. The mass loss of the specimens during the wear test was measured using electronic weighing machine before and after the experiment.

The Pin-on-disc wear test machine which is used in the present wear study has linear variable differential transducer (LVDT) and load cell. This LVDT continuously monitor the wear depth of specimen through the connected sensor which is mounted on the plunger. The normal load is applied on the specimen by the loading lever which is pivoted at one point. The distance between the sensor and lever pivot point is maintained same as that the distance between the specimen and lever pivot point to get accurate result. The plunger is rest on the projection from the loading lever. The movement of the loading lever indicates the wear of specimen. Based on this arrangement, the plunger moves according to the movement of loading lever. The LVDT sense the plunger movement and display on the controller. The frictional force is measured by the load cell which is mounted on the bracket. The distance between the bracket and lever pivot point is same as that the distance between the specimen and lever pivot point. This load cell is a foil type strain gauge which deform minutely even at the low load condition. It is connected with the balanced wheat stones bridge and produce the electrical output whenever the strain gauge is deformed. The produced electrical output is directly proposal to force acting on the strain gauge. The controller decodes the data and display the information online in the form of friction force vs sliding time and wear depth vs sliding time. From these data, CoF and wear rate were obtained by equation 1 and 2, respectively and plotted against the sliding time. The wear mechanisms were studied by analyzing the worn-out surfaces through FESEM images. The surface roughness of worn surfaces was measured using white-light interferometer (MFT-5000, Rtec Instruments, USA).

$$\text{Wear rate of Pin} = \frac{\text{wear depth X crosectional area of Pin}}{\text{sliding distance}} \left(\frac{\text{mm}^3}{\text{m}} \right) \quad (1)$$

$$\text{CoF of Pin} = \frac{\text{Friction force}}{\text{Normal load}} \quad (2)$$

3. Results and discussion

3.1. Microstructure analysis

Uniform mixing of Co, Fe, Cr, Al, Cu and Ni HEA elements are observed in the FESEM image of resultant ball milled powder mixture as shown in Fig. 2a. EDS analysis of powder revealed the presence of all elements and their atomic weight ratio as shown in Fig. 2b. The cross-section of PTA alloyed surface is shown in Fig. 3. The optimal PTA process parameters were identified based on the defect-free surface and alloyed depth with good metallurgical bonding. The base material has a dual-phase microstructure with bright field of α phase and dark field of β phase as shown in Fig. 4a. The PTA alloyed surface exhibited dendritic and interdendritic structure as shown in Fig. 4b. The PTA alloying process was performed at the optimal process condition which reduced the crack formation tendency. As a result, crack-free PTA alloyed surface was observed in Fig. 4b to 4d.

EDS analysis was performed at the top and near interface region of PTA alloyed surface which is marked in red color dotted line in Fig.4b and results are shown in Fig. 4e and 4f, respectively. The quantitative value of the alloying elements in the alloyed region is shown in Table 3. The EDS results showed that the presence of Al element is higher than the other alloying elements in the top and near the interface region of the alloyed region. The dilution effect of the PTA alloying process was caused by the thermal input, which made the Al penetration into the alloyed region from the base material. It led to the mixing of more Al element in the alloyed region. Al element promoted the formation of stronger p-d orbital bonding with other alloying elements as it has incompletely filled d-shell to increase the slip resistance [23]. Furthermore, the increase of Al content suppresses the formation of a central cluster and stabilizes a chemically ordered BCC phase. As a result, the BCC phase was formed in the major region of the alloyed region. The presence of Ni-rich phases indicates that some FCC phases are also formed in the alloyed region. Chromium has a melting point of 1907°C which is higher than the melting point of Fe, Co, Ni, Cu, Ti and Al elements. As a result, its diffusivity is lower than that of the other elements which leads to the lower content of chromium element in the alloyed region.

TABLE 3

EDS analysis results of PTA alloyed HEA coating at different region

EDS analysis results (in Atomic wt.%)	Cr	Co	Cu	Fe	Ni	Al
Top region [Fig. 4(e)]	13.41	22.35	8.92	12.71	13.72	28.89
Near the intersection region [Fig. 4(f)]	12.45	15.28	9.78	10.41	16.07	36.01
Dark region [Fig. 4(g)]	3.86	12.79	13.24	7.44	17.00	45.86
White region [Fig. 4(h)]	7.23	3.89	10.27	4.63	3.96	70.01

Dark and white particles are observed in Fig. 4d. EDS analysis was performed in the dark and white region, which is shown in Fig. 4g and 4h, respectively. Dark region has major ele-

ments of Al, Ni and Cu whereas white region has Al rich region. Dark region possessed both FCC and BCC phases whereas the white region has BCC phases. NiAl phase was formed due to the larger negative mixing enthalpy of –22 kJ/mol. Moreover, the Fe element prefers the Al sites whereas Cr and Co elements prefer the Ni sites in the NiAl phase. As a result, this phase consists of Co, Fe, Cu and Cr along with the NiAl phase. Dendritic regions formed as a continuous structure and constituted large volume fraction of microstructure, whereas interdendritic regions have formed as a discontinuous structure.

The segregation of Cu elements in the boundary was due to the positive mixing enthalpy of Cu with other elements which led to the repulsion between Cu atoms and the rest of HEA ele-
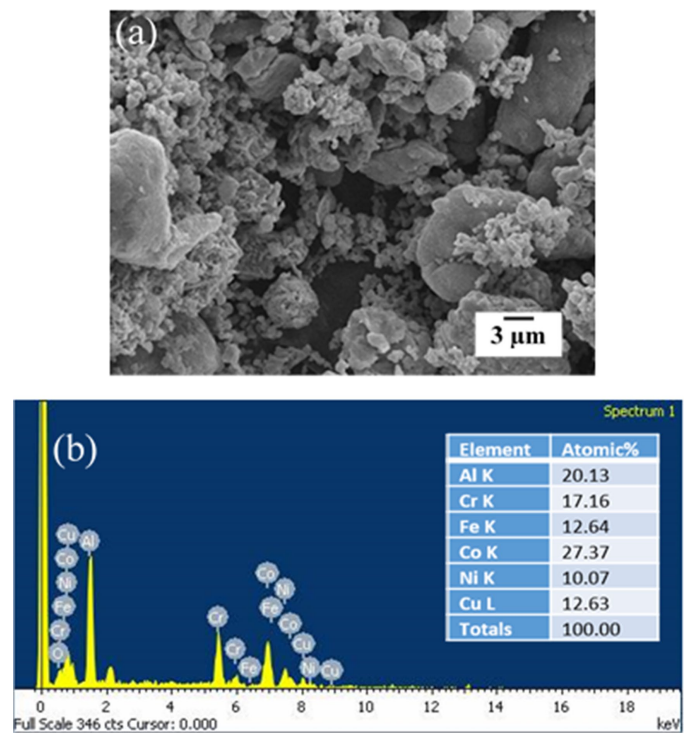

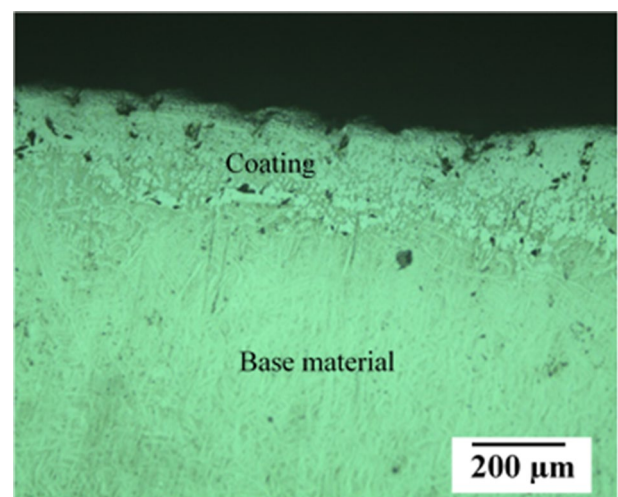Fig. 2. AlCrFeCuCoNi HEA alloy powders (a) FESEM image (b) EDS analysis with atomic Percentage

Fig. 3. Cross sectional Optical microscopy (OM) image of PTA alloyed region

ments. The pair of elements such as Cu-Fe, Cu-Co and Cu-Cr need larger mixing enthalpy than Cu-Ni and Cu-Al pairs, leading to the less Fe, Co and Cr content than other elements such as Al, Ni and Cu in the boundary region. Segregation of Ni, Co, Cr, Fe and Al is small in the PTA alloy due to negative mixing enthalpy of alloying elements. The mixing enthalpy of Co-Cr, Cr-Al, Ni-Co, Co-Al, Ni-Cr, Ni-Fe, Ni-Al, Co-Fe, Cr-Fe, Fe-Al are –4, –10, 0, –19, –7, –2, –22, –1, –1 and –11, respectively [18]. The alloy system AlCoCuFeNi combination induced the FCC phase whereas the addition of Cr element converted this FCC phase to the BCC phase. As a result, the dominant BCC phase was formed on AlCoCuFeNiCr alloyed surface [24-26]. The slip along the BCC plane is more difficult when compared to that of FCC planes due to more irregular arrangement than
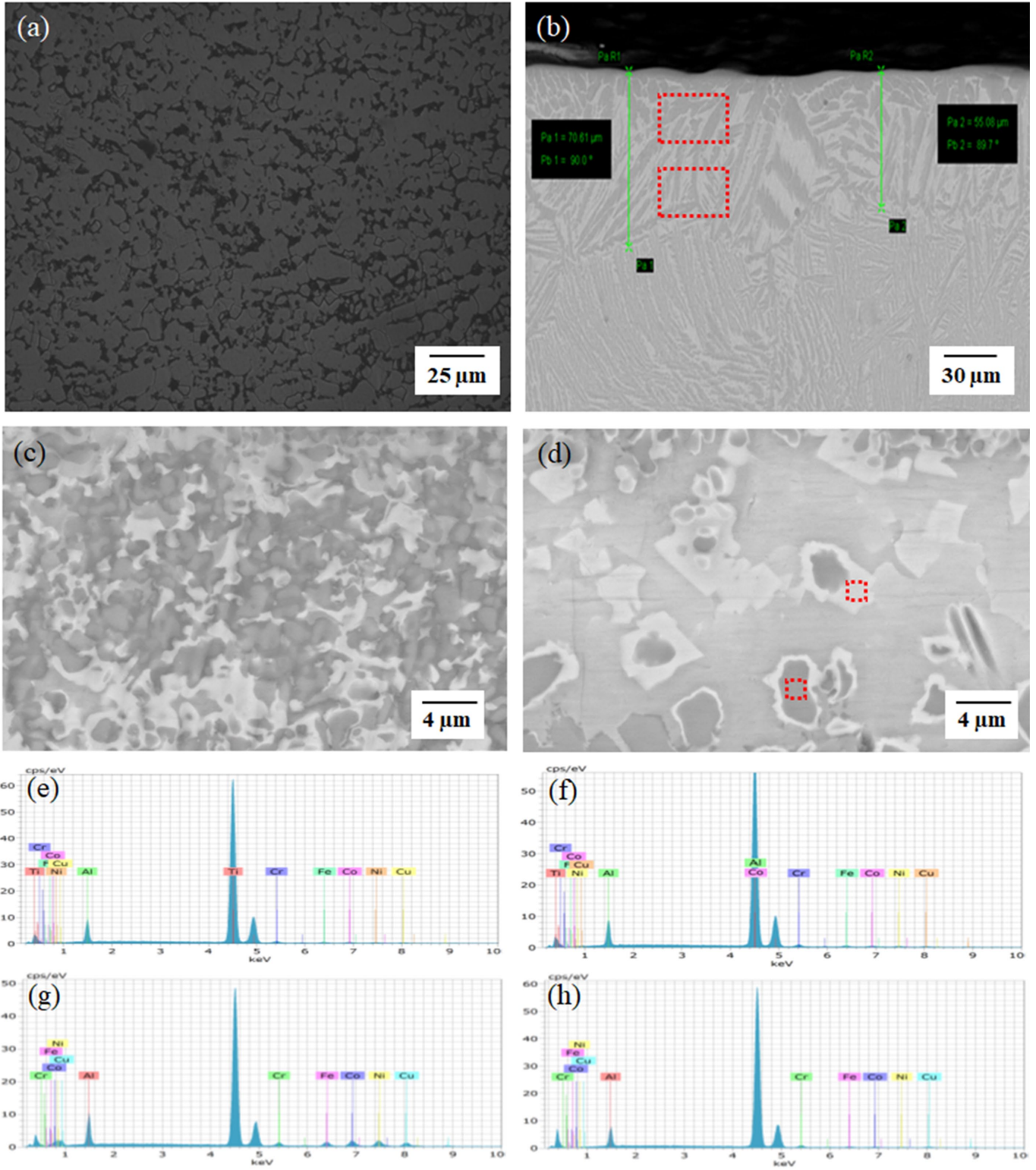

Fig. 4. FESEM image of (a) Ti-6Al-4V base material (b) PTA alloyed cross section, (c) & (d) magnified images of PTA alloyed surface, EDS analysis result of (e) alloyed top region, (f) alloyed near interface region, (g) dark region (h) white region

FCC plane. BCC phase has small interplanar distance and high lattice friction. It incorporated more Al element and Cr elements which has strong binding force with other alloying elements and enhance the slip resistance. As a result, higher hardness was obtained in BCC phase than FCC phase. Plasticity of alloyed samples decreased as the BCC phase has less slip direction than the FCC phase. Alloyed surface enhanced the hardness with the BCC phase.

Microstructure of the alloyed region depends on the formation of the temperature gradient. Planar growth occurs at the interface between the base material and the molten pool at higher value of the ratio of temperature gradient and growth rate. The ratio of temperature gradient and growth rate decreases from the solid-liquid interface to the center of the molten region. As a result, the microstructural formation changed from planar grains to columnar grains which occurred in the direction perpendicular to the interface of base material and alloyed region [27-28]. The decomposition of a supersaturated solid solution takes place at lower cooling rates and results in different phase formation. As a result, BCC, FCC and few intermetallic compounds are formed in PTA alloying region.

The EDS elemental mapping was performed on the alloyed region which is shown in Fig. 5. The results showed that all alloying elements were presented and distributed throughout the alloyed region. Macro segregation of HEA elements were not observed in the alloyed region.

3.2. Phase analysis

The XRD spectrum of HEA powder and PTA alloyed sample composed of FCC and BCC phase as shown in Fig. 6. Phases of PTA alloyed samples differ from HEA powder due to the presence of base material elements. Formation of FCC and BCC phases were promoted through Cu, Co, Ni element and Al, Fe, Cr elements, respectively [29]. In addition, fast cooling rate during the PTA process induced the FCC phase and promoted the formation of disordered BCC phase [30]. The intensity of the BCC phase was much stronger than the FCC phase, which revealed that the BCC phase occupied more volume fraction than the FCC phase. Ti and Al elements from the base material were mixed with the alloyed region at the non-equal atomic ratio which produced some intermetallic compounds such as TiNi, Al_3Ti and Cr_2Ti. The addition of vanadium has not shown any effect on the improvement of the intensity of phases. The XRD peaks of each individual ingredient element was shifted owing to the effects of solid solution intensity. Based on Boltzmann's theory, higher disorder and lower segregation of AlCoCrCuFeNi alloying were achieved on PTA alloyed surface [14,31]. Lattice distortion has occurred during the HEA alloyed region which minimized the formation of crystalline structure and increased the random distribution of atoms. As a result, heights of the diffraction peaks reduced in the alloyed region.
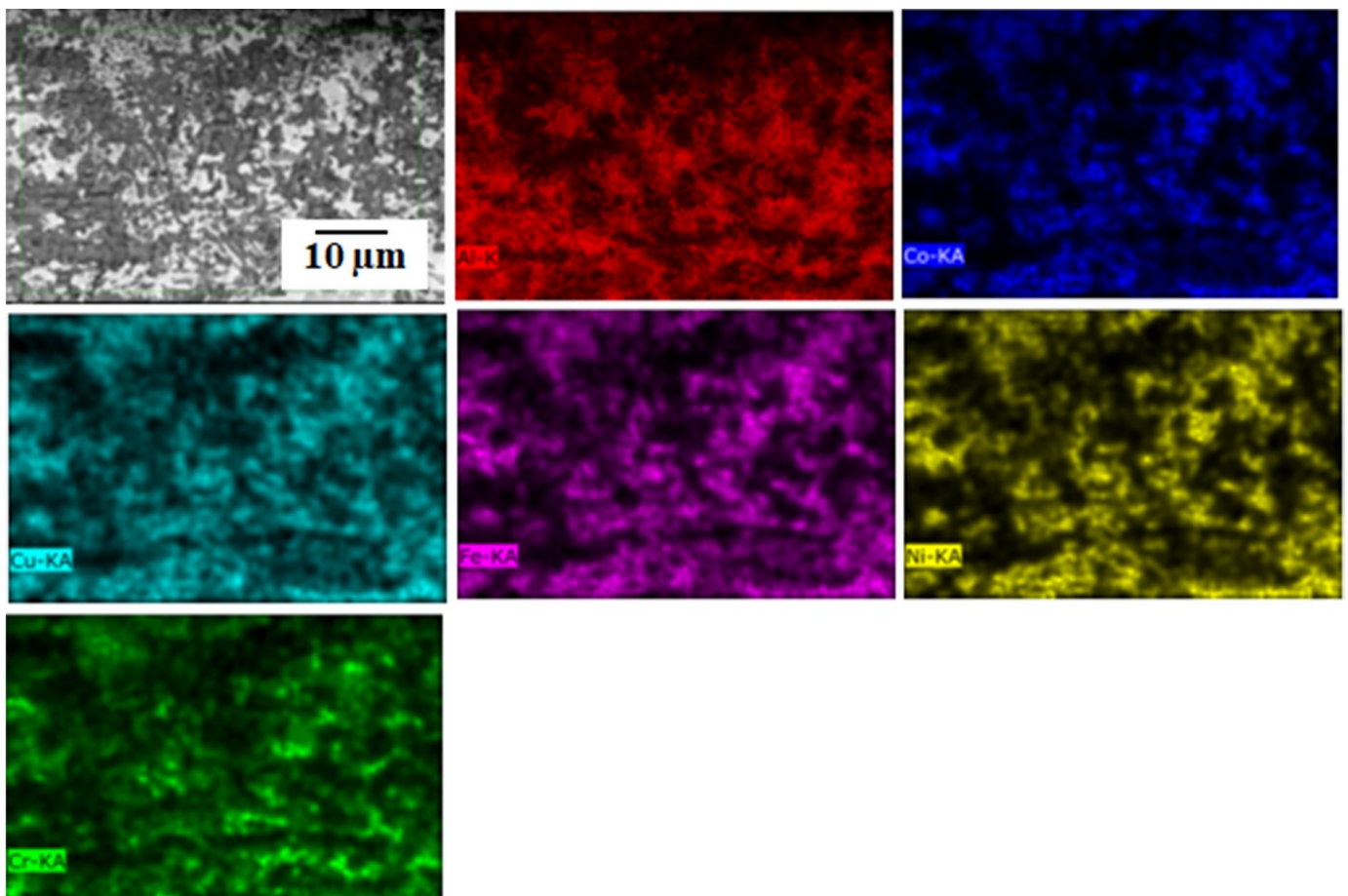

Fig. 5. EDS elemental mapping of Al, Co, Cu, Fe, Ni and Cr elements in the HEA PTA alloyed region
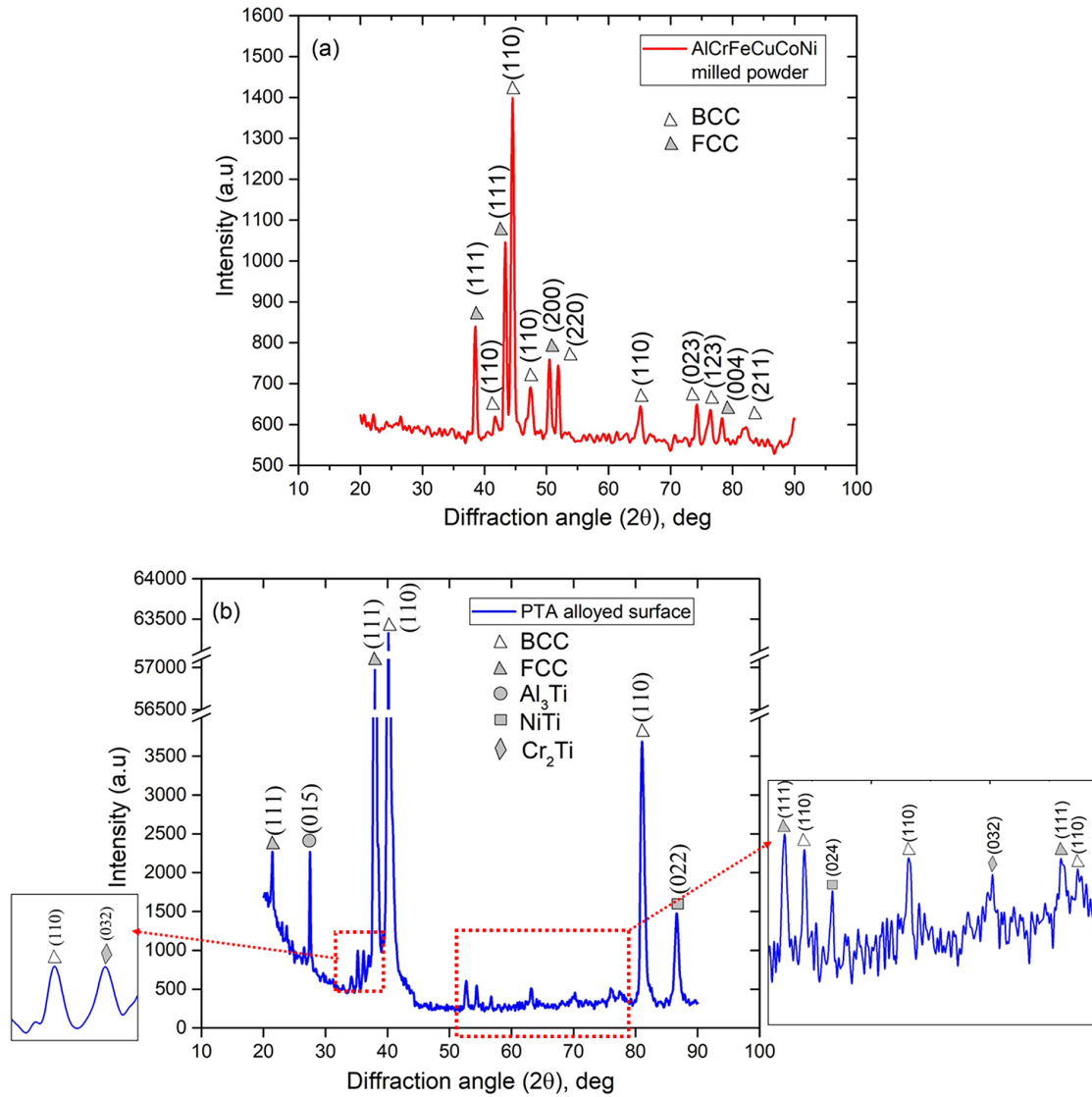
Fig. 6. XRD spectrum of (a) AlCrFeCuCoNi milled powder (b) PTA alloyed surface

3.3. Microhardness examination

The microhardness at the cross-section of PTA alloyed zone, interface zone and base material were plotted and is shown in Fig. 7. The measured hardness shows that the PTA alloyed surface has higher hardness compared to the base material. In PTA specimen, the measured average hardness in the alloyed and heat-affected zone are 718 $HV_{0.2}$ and 330 $HV_{0.2}$, respectively. The hardness measured across the alloyed zone of the PTA modified surface is twice than the base material. The increased hardness on the PTA surface was attributed to the solution strengthening and grain refinement effect [32]. Microhardness of the PTA surface was enhanced due to the uniform fusion of HEA particles to the base material [33]. The OM picture of indentation marks which were captured during the hardness measurement were inserted in the hardness profile. It can be observed that the indentation size is lesser in PTA alloyed surface compared to the interfacial zone. The interface region size of the base material is larger than both the PTA surface and the interfacial layer. The lesser
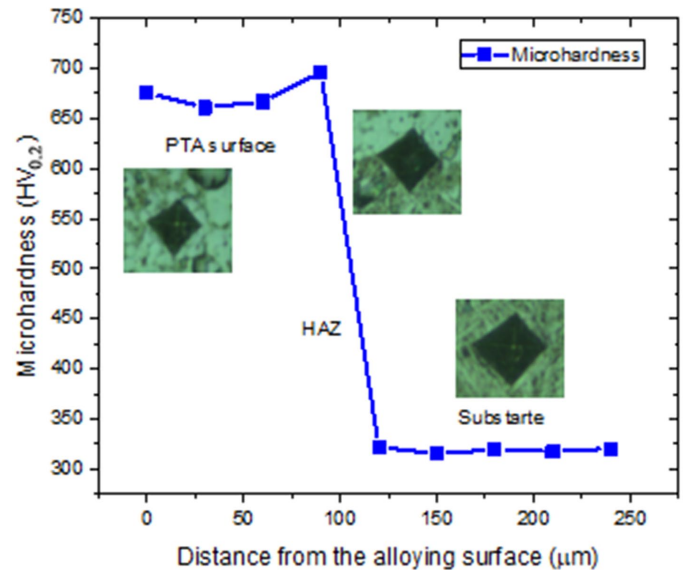

Fig. 7. Microhardness of PTA alloyed sample with optical microscope images of indentation marks at three different regions

indentation size proves that the PTA alloyed surface has capable of withstanding maximum loads compared with greater marks when performing with similar loads in both regions.

3.4. Friction and wear behaviour

The measured Coefficient of Friction (CoF) values were plotted against the sliding time for both base material and PTA alloyed samples which are shown in Fig. 8a and 8c, respectively. The base material exhibited the CoF of 0.46 and 0.56 at wear parameters of 35 N load with the sliding velocity of 1.2 m/s and 50 N load with the sliding velocity of 0.9 m/s, respectively. However, PTA alloyed sample exhibited the CoF of 0.35 and 0.44, respectively which shows that the lower and stable friction coefficient has occurred compare to the performance of the base material. The oxide film plays an important role in reducing the CoF. As reported elsewhere, oxide film has formed on the base material which was broken during the wear test as the thickness of oxide film is in nanometre level [34]. The CoF of base material increased drastically than the PTA alloyed sample. Frictional heat produced during the wear test has promoted the formation of FeO, Cr_2O_3, NiO and Al_2O_3 oxide film on the PTA alloyed sample [35]. Moreover, the Cu element has a high repulsion effect with other alloying elements and segregated at the dendrite and inter-dendrite regions [36]. The segregated Cu

reacted with the atmosphere oxygen, resulted in the formation of copper oxide which was part of the oxide layer between the mating parts. Consequently, it reduced the CoF of the PTA alloyed sample. Verma et al. [37] added the Cu elements in the CoCrFeNi HEA matrix and found the reduction of CoF due to the formation of Cu oxide. Hence, the oxide film of AlCoCr-CuFeNi HEA had acted as a lubricant film which leads to the decrease in the CoF of the PTA alloyed sample. Moreover, a stable CoF had occurred due to the formation of a dynamic equilibrium between growth and broken-out of oxide film [38]. It diminished the adhesion of the PTA alloyed sample to the counter body.

Wear resistance of base material and PTA alloyed samples were investigated under dry sliding conditions and the results are shown in Fig. 8b and 8d, respectively. The PTA alloyed AlCrFeCuCoNi HEA coating has higher wear resistance than the base material at both wear parameters. The PTA alloyed sample has higher wear resistance at 35 N load with the sliding velocity of 1.2 m/s than the wear resistance at 50 N load with the sliding velocity of 0.9 m/s due to increase in load and decrease in sliding velocity. Base material has lower wear resistance at 50 N load with the sliding velocity of 0.9 m/s than the wear resistance at 35 N load with the sliding velocity of 1.2 m/s. Wear resistance of PTA alloyed sample was increased due to higher binding force of Ni, Co, Cr and Fe elements and higher hardness of PTA alloyed sample as per Archard's law [39].
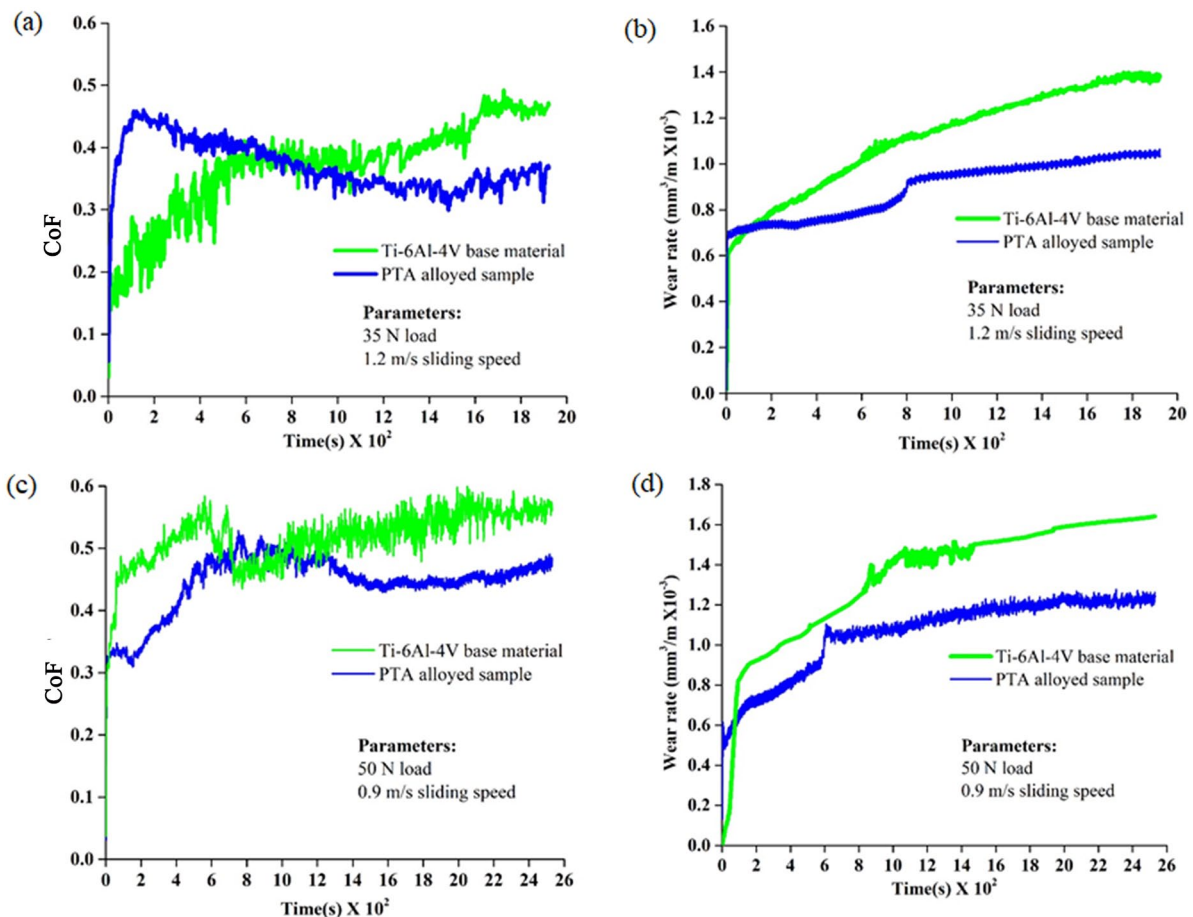

Fig. 8. (a and c) Coefficient of Friction (CoF), (b and d) wear behaviour for base material and PTA alloyed samples, respectively

3.5. Wear mechanism

Wear tracks of base material and PTA alloyed samples were analysed by FESEM image as shown in Fig 9. Deep grooves, craters, debris and plastic deformation are observed on the base material surface under both wear conditions (Fig. 9a and 9b). Base material had lost more material due to the formation of deep grooves as micro-cutting has predominantly occurred. It shows that the abrasive wear was occurred on it which resulted in a rough surface [40]. Moreover, the base material has an unstable CoF due to severe scuffing between the mating surface of base material and counter body.

Small wear grooves were present on PTA alloyed samples with negligible amount of spalling. This can be explained by the better interconnection of the coated material and superior metallurgical bonding to the base material (Fig. 9c and 9d). Moreover, wear resistance of PTA alloying has enhanced due to solid solution strengthening process as the HEA has high entropy of mixing which leads to the reduction of free energy of the alloyed region [41]. The hardness was increased during the PTA alloyed region which enhanced the wear resistance and reduced the pit formation on the alloyed region. The strength of the alloyed region is far higher than that of shear force. The hard phases were formed in the alloyed region due to the inclu-
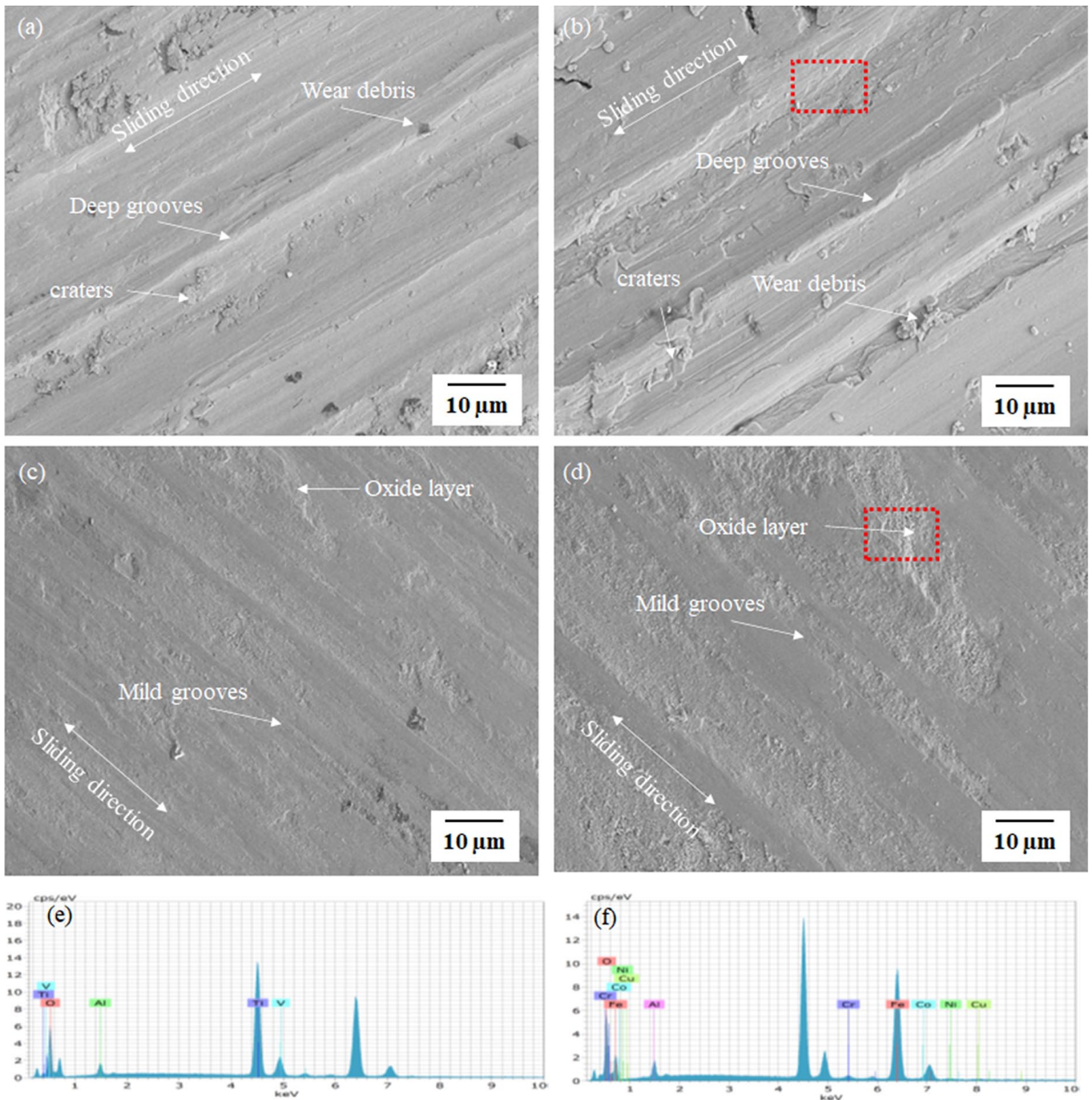

Fig. 9. FESEM images of worn out surface; (a-b) Base material specimen with 35N and 50 N load, respectively. (c-d) PTA alloyed specimen with 35 N and 50 N load, respectively, (e-f) EDS analysis result at red mark in (b) and (d) respectively.

sion of Ti element from the base material to the alloyed region. It is difficult to wear out the hard phases. However, hard phases were brittle in nature and pulled out under the impact of the wear counterpart. This may produce some pits in the worn-out surface of the alloyed region. Moreover, Ni, Co, Cr and Fe elements have higher binding force with each other [42]. Large lattice distortion occurred in the alloyed region due to significant variation in the atomic radius of HEA elements as the atomic radius of the HEA elements Al, Fe, Cu, Cr, Co and Ni are 143, 126, 140, 128, 125 and 124 (pm), respectively [43]. These binding energy between the elements and lattice distortion leads to the strengthening of the PTA alloyed material. It restricted the deformation of material during the wear test and reduced the material loss.

EDS analysis was performed on the worn-out surface and the results are included in Table 4. The worn-out base material shows higher amount of Ti element with small amount of Al, V and oxygen elements. The worn-out PTA alloyed region exhibited higher Fe elements which were transferred from the counter body. Presence of oxygen on the PTA alloyed region is higher than the base material. It shows that the oxides were formed on the worn-out surface of PTA alloyed region. Schematic representation of wear mechanism is shown in Fig. 10. Fine microstructure was formed in the PTA alloyed region due to the rapid solidification of alloying elements. High-temperature stability and higher hardness of the alloyed region reduced the plastic deformation which leads to lower wear rate and CoF [44]. Besides, oxide film has formed at the PTA alloyed surface that act as a barrier between two matting surfaces and reduced the direct contact of PTA region with the mating surface [45]. As a result, wear and friction between the mating parts get reduced. Elastic deformation can be recovered which is induced by external stresses.

3.6. Whitelight interferometer analysis

Fig. 11 shows the three-dimensional profile and corresponding two-dimensional diagram of the abraded base material and PTA alloyed samples under 50 N load with 0.9 m/s sliding velocity. The dark stripes observed in the three-dimensional image of a base material are corresponds to grooves. It revealed that the abraded surface of base material had a greater number of parallel wide deep grooves in the sliding direction, some discontinuous grooves, dents and humps. Whereas, PTA alloyed sample possess parallel grooves with decreasing width and depth and some debris due to fracture of solid surface. As a result, the worn-out surface of base material had higher surface roughness (Ra) of 5.30 μm than the surface roughness of the PTA alloyed sample of 2.86 μm. It shows that the surface roughness of the PTA alloyed sample was 0.46 times lower than the base material due to the higher hardness of the PTA alloyed sample than the base material. It reveals that the PTA alloyed sample has a lower depth of wear than the base material.

4. Conclusions

AlCrFeCuCoNi HEA was surface alloyed on Ti-6Al-4V using PTA alloying. Tribological property of PTA alloyed samples at two different wear parameters were studied and the following conclusions are derived based on the experimental results.
- PTA alloyed surface has pore free microstructure with columnar dendritic BCC structure and interdendritic FCC structure due to the influence of phase stabilizers such as Al, Fe, Cr, Ti and Cu, Co, Ni elements.

TABLE 4

EDS analysis results of worn-out surface of Base material and PTA alloyed HEA coating

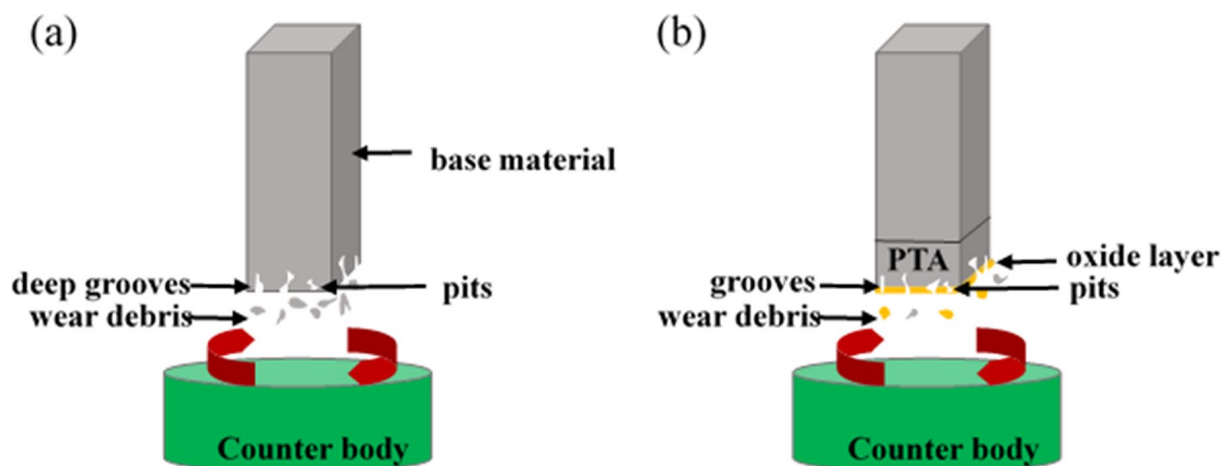| EDS analysis results (in Atomic wt.%)	Ti	Al	V	O	Fe	Cr	Co	Cu	Ni
Base material [Fig. 9(e)]	78.74	5.72	3.67	11.87	—	—	—	—	—
PTA alloyed region [Fig. 9(f)]	30.31	11.41	1.05	21.92	8.47	3.57	7.12	6.23	9.92

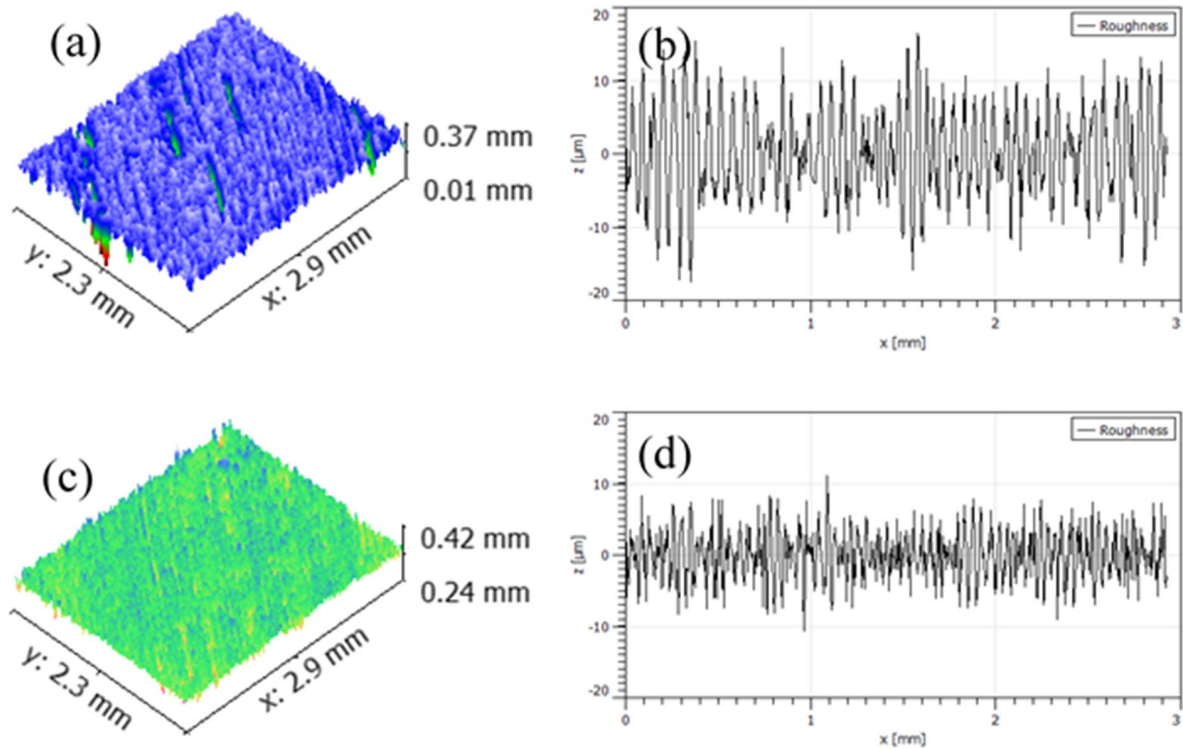Fig. 10. Schematic representation of wear mechanism (a) base material (b) PTA alloyed sample

Fig. 11. (a) and (b) 3D topography of worn out surfaces and its roughness plot of base material at 50N load; (c) and (d) 3D topography of worn out surfaces and its roughness plot of PTA alloyed sample at 50 N load

- HEA elements enhanced the lattice distortion of the alloyed region which resulted in broadening of the BCC phase in the alloyed region than the AlCrFeCuCoNi HEA powder.
- PTA alloyed region possess some intermetallic compounds such as $TiNi$, Al_3Ti and Cr_2Ti due to nonequal molar mixing of Ti and Al elements from the base material.
- Superior solution strengthening and higher slip resistance have occurred in the alloyed region because of the inherent property of HEA elements which led to the increase in microhardness of the alloyed region.
- PTA alloyed sample has higher wear resistance than the base material due to higher binding force of Ni, Co, Cr and Fe elements, which resulted in more lattice distortion and restricted the deformation of material during the wear test.
- HEA particles promoted the formation of oxide film on the PTA alloyed region which acted as a barrier between two contact surfaces and reduced the friction of the PTA alloyed sample.
- The surface roughness of the worn-out PTA alloyed sample was lower than the base material due to the higher hardness and good metallurgical bonding of coating with the base material.

REFERENCE

[1] M. Krol, T. Tanski, Arch. Metall. Mater. **61**(3), 1291-1296 (2016).

[2] J. Marciniak, J. Szewczenko, W. Kajzer, Arch. Metall. Mater. **60**(3), 2123-2129 (2015).

[3] Yunlong Zhang, Jun Li, Yunqiang Jiang, Danning Kang, Yongfei Juan, Zhongjie Lu, Mater. Res. Express (2020). DOI: https://doi.org/10.1088/2053-1591/ab6a53 (in press).

[4] J. Zhang, S. Xue Li, Appl. Surf. Sci. **280**, 626-631 (2013).

[5] D. Er, G.T.P. Azar, M. Kazmanlı Kand Ürgen, Surf. Coat. Technol. **346**, 1-8 (2018).

[6] W. Liu, S. Liu, L. Wang, Coatings **9**, 1-23 (2019).

[7] W. Chen, W. Gao, Electrochim. Acta **55**, 6865-6871 (2010).

[8] Tae Hyun Park, Min Seok Baek, Yongho Sohn, Kee Ahn Lee, Arch. Metall. Mater. **65**(3), 1073-1080 (2020).

[9] Youlu Yuan, Zhuguo Li, Surf. Coat. Technol. **248**, 9-22 (2014).

[10] Youlu Yuan, Zhuguo Li, Appl. Surf. Sci. **423**, 13-24 (2017).

[11] R.P. Garcia, S.C. Canobre, H.L. Costa, Tribol. Int. **143**, 106080 (2020).

[12] L. Baiamonte, M. Tului, C. Bartuli, D. Marini, A. Marino, F. Menchetti, R. Pileggi, G. Pulci, F. Marr, Surf. Coat. Technol. **371**, 322-332 (2019).

[13] H.T. Cao, X.P. Dong, Z. Pan, X.W. Wu, Q.W. Huang, Y.T. Pei, Mater. Des. **100**, 223-234 (2016).

[14] Jien Wei Yeh, Swe Kai Chen, Su-Jien Lin, Jon Yiew Gan, Tsung Shune Chin, Tao Tsung Shun, Chun Huei Tsau, Shou Yi Chang, Adv. Eng. Mater. **6**, 299-303 (2004).

[15] Dechao Zhao, Tomiko Yamaguchi, Wenqin Wang, Mater. Lett. (2019). DOI: https://doi.org/10.1016/j. matdes.2020.108872 (in press).

[16] Hao Liu, Jian Liu, Peijian Chen, Haifeng Yanga, Opt. Laser Technol. **118**, 140-150 (2019).

[17] J. Huebner, P. Rutkowski, D. Kata, J. Kusinski, Arch. Metall. Mater. **62** (3), 531-538 (2017).

420

[18] Kaijin Huang, Yuyue Wang, Xin Lin, Adv. Mater. Res. **989-994**, 246-250 (2014).

[19] Guo Jin, Zhaobing Cai, Yajie Guan, Xiufang Cui, Zhe Liu, Yang Li, Meiling Dong, Dan zhang, Appl. Surf. Sci. **445**, 113-122 (2018).

[20] Benbin Xin, Youjun Yu, Jiansong Zhou, Lingqian Wang, Shufang Ren, Surf. Coat. Tech. **313**, 328-336 (2017).

[21] Jiasi Luo, Songquan Wu, Yanjin Lu, Sai Guo, Yang Yang, Chaoqian Zhao, Junjie Lin, Tingting Huang, Jinxin Lin, J. Mater. Sci. Mater. Med. **29**, 37-46 (2018).

[22] ASTM G99-05, Standard Test Method for Wear Testing with a Pin-on-Disk Apparatus, ASTM International, Ohio (2010).

[23] Wei Lia, Ping Liua, Peter K. Liawb, Mater. Res. Lett. **6** (4), 199-229 (2018).

[24] L.J. Santodonato, Y. Zhang, M. Feygenson, C.M. Parish, M.C. Gao, M.K. Miller, R.J.K. Weber, J.C. Neuefeind, Z. Tang, P.K. Liaw, Nat. Commun. (2015).
DOI: https://doi.org/10.1038/ncomms 6964 (in press).

[25] Y. Zhang, T.T. Zuo, Z. Tang, M.C. Gao, K.A. Dahmen, P.K. Liaw, Z.P. Lu, Prog. Mater. Sci. **61**, 1-93 (2014).

[26] C.C. Tung, J.W. Yeh, T.T. Shun, S.K. Chen, Y.S. Huang, H.C. Chen, Mater. Lett. **61**, 1-5 (2007).

[27] L. Arnberg, R. H. Mathiesen, Mater. Forum **28**, 47-52 (2004).

[28] M.L. Melo, E.M.S Rizzo, R.G. Santos, Mat. Sci. Eng. A Struct. **374**, 351-361 (2004).

[29] Jin Ming Zhu, Jie Li Meng, Rare Met. **35** (5), 385-389 (2016).

[30] Martin Lobel, Thomas Lindner, Thomas Lampke, Materials (2018). DOI: https://doi.org/10.3390/ma 11112225 (in press).

[31] J.W. Yeh, Ann. Chim. Sci. Mat. **31**, 633-648 (2006).

[32] Mohammed Mohaideen Ferozhkhan, Muthukannan Duraiselvam, Kottaimathan, Ganesh kumar, Rajanbabu Ravibharath, Proc. Technol. **25**, 1305-1311 (2016).

[33] Tiago Jose Anto, Rodrigo Metz Gabriel Paes, Ana Sofia Clímaco Monteiro de Oliveira II, Adriano Scheid, Soldag. Insp. **19**, 134-144 (2014).

[34] K.M. Li, K.J. Songc, J. Guan, F. Yang, J. Liu, Surf. Coat. Technol. (2020). DOI: https://doi.org/10.1016/j.surfcoat.2020.125506 (in press).

[35] Peiying Shi, Yuan Yu, Nina Xiong, Mingzi Liu, Zhuhui Qiao, Gewen Yi, Qianqian Yao, Gaopan Zhao, Erqing Xie, Qihua Wang, Tribol. Int. **151**, 106470 (2020).

[36] T.M. Yue, H. Xie, X. Lin, H.O. Yang, G.H. Meng, J. Alloys Compd. **587**, 588-593 (2014).

[37] A. Verma, P. Tarate, A.C. Abhyankar, M.R. Mohape, D.S. Gowtam, V.P. Deshmukh, T. Shanmugasundarama, Scr. Mater. **161**, 28-31(2019).

[38] Jin Kun Xiao, Hong Tan, Yu Qing Wu, Juan Chen, Chao Zhang, Surf. Coat. Technol. **385**, 125430 (2020).

[39] Caiyun Shang, Eugen Axinte, Wenjuan Ge, Zitang Zhang, Yan Wang, Surf. Interfaces **9**, 36-43 (2017).

[40] Shreyash Hadke, Rajesh K. Khatirkar, Satish K. Shekhawat, Shreyans Jain, Sanjay G. Sapate, J. Mater. Eng. Perform. **24**, 3969-3981 (2015).

[41] T.M. Yue1, G.H. Meng, H. Xie, X. Lin, H.O. Yang, Int. J. Metall. Mater. Eng. **1**, 115 (2015).

[42] J.B. Cheng, X.B. Liang, Z.H. Wang, B.S. Xu, Plasma Chem. Plasma Process. **33**, 979-992 (2013).

[43] S. Zhang, C.L. Wu, C.H. Zhang, M. Guan, J.Z. Tan, Opt. Laser Technol. **84**, 23-31 (2016).

[44] Yue Zhang, Zheng Chen, Dongdong Cao, Jinyong Zhang, Ping Zhang, J. Mater. Res. Tech. **8**, 726-736 (2019).

[45] Aijun Zhang, Jiesheng Han Bo Su, Pengde Li, Junhu Meng, Mater. Des. **114**, 253-263 (2017).